

BOOK OF TUTORIALS AND ABSTRACTS



European Microbeam Analysis Society

EMAS 2009

11th

EUROPEAN WORKSHOP

on

MODERN DEVELOPMENTS

AND

APPLICATIONS

IN

MICROBEAM ANALYSIS

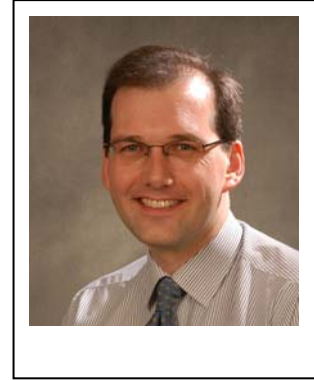
10 to 14 May 2009

at the

Hotel Spa Faltom

Gdynia/Rumia, Gdansk, Poland

Organized in collaboration with
Silesian University of Technology
Polish Society for Microscopy (PTMi)
Polish Academy of Sciences:
Committee of Materials Science, Institute of Physics,
Institute of Materials Science and Metallurgy



NANOSCALE ANALYSIS IN 3D USING ELECTRON TOMOGRAPHY

Paul A. Midgley

University of Cambridge, Department of Materials Science and Metallurgy
Pembroke Street, Cambridge CB2 3QZ, Great Britain

Paul A. Midgley is Professor of Materials Science and Director of the Electron Microscope Facility at the Department of Materials Science and Metallurgy in the University of Cambridge. He obtained his first degree and Ph.D. at the University of Bristol where he remained as an 1851 Research Fellow and then as a Royal Society Research Fellow. He moved to Cambridge in 1997.

He has studied a wide variety of materials by electron microscopy and has developed a number of novel electron microscopy techniques, including new micro-analytical techniques using energy-filtered transmission electron microscopy (EFTEM) and scanning transmission electron microscopy (STEM), and the introduction and development of electron tomography in materials science. He is Editor-in-Chief of the journal *Ultramicroscopy*. He was the 2004 Federation of European Materials Societies (FEMS) Lecturer and recipient of the Institute of Materials Rosenhain Medal in 2004. He was awarded a Royal Academy of Engineering / Leverhulme Trust Senior Research Fellowship for 2005/6. He won the Ernst-Ruska Prize awarded by the German Microscopy Society in 2007. In August 2008, he was elected President of the *European Microscopy Society*.

1. INTRODUCTION

The increasingly important roles that nanoscience and nanotechnology play in the development of modern devices and structures means that characterization techniques are needed that are capable of providing quantitative information with nanometre resolution. The TEM has provided an excellent tool to do this for decades but as devices and materials become more complex there is a pressing need to examine structures also in three dimensions. Electron tomography using the TEM enables a full 3D reconstruction of the object of interest with high spatial resolution. Not only is the morphology reconstructed but information about the composition and chemistry, defect structure and physical properties may be determined.

2. TOMOGRAPHY

Although the theoretical principles behind tomography can be traced back to 1917 [1], it was only in 1956 [2] when the idea was proposed for a practical application – to reconstruct a 2D map of solar emission from a series of 1D ‘fan beam’ profiles measured by a radio telescope. From 1963 onwards [3] the X-ray computerized tomography (CT) scanner [4] was developed, for which Cormack and Hounsfield, were awarded the Nobel Prize for Medicine in 1979. Electron tomography started with the publication of three key papers in 1968: (i) by de Rosier and Klug [5], using Fourier reconstruction methods to determine the helical structure of a biological macromolecule from a single micrograph; (ii) by Hoppe [6], who showed that given a sufficient number of projections it should be possible to reconstruct fully asymmetrical systems; and (iii) by Hart [7], who demonstrated that the image signal to noise ratio could be improved using an ‘average’ re-projected image calculated from a tilt series of micrographs, a technique Hart called a polytropic montage. Whilst electron tomography, in its various forms, has been exploited very successfully in the life sciences, it is only in the last 5 - 10 years that electron tomography has gained prominence in the physical science community, partly through the introduction of new imaging modes and partly through the introduction of computer-controlled microscopes with high precision goniometers and advances in computing power that enable reconstructions to be achieved in minutes rather than days.

3. FUNDAMENTALS OF TOMOGRAPHIC RECONSTRUCTION

In Radon’s original paper [1], the (now-called) Radon transform, R , is defined as the mapping of a function $f(x,y)$, describing a real space object D , by the projection, or line integral, through f along all possible lines L with unit length ds so that,

$$Rf = \int_L f(x,y)ds \tag{1}$$

A discrete sampling of the Radon transform is geometrically equivalent to the sampling of an object by a projection or transmitted signal and therefore the structure of an object $f(x,y)$ can be reconstructed from projections Rf using the inverse Radon transform. A series of projections at different angles will therefore sample Radon space and, given a sufficient number of projections, an inverse Radon transform of this space should reconstruct the object. In practice the sampling will be limited and any inversion will be imperfect. The goal of any reconstruction then becomes achieving the ‘best’ reconstruction of the object given the limited experimental data.

A projection of an object at a given angle in real space corresponds to a central section through the Fourier transform of that object – the ‘central slice theorem’ [8]. By recording multiple images (projections) at different angles many Fourier sections will be sampled and tomographic reconstruction is possible from an inverse Fourier transform of the set of Fourier transformed projections [8, 9]. Although elegant, Fourier reconstruction methods are computationally intensive and difficult to implement for electron tomography and have largely been superseded by faster and simpler real space ‘back-projection’ methods [8, 10, 11]. The method of back-projection is based on ‘smearing’ the image into an object space at the angle of the original projection. With a sufficient number of back-projections from different angles, the superposition of all the backprojected ‘rays’ will return the original object, see Fig. 1.

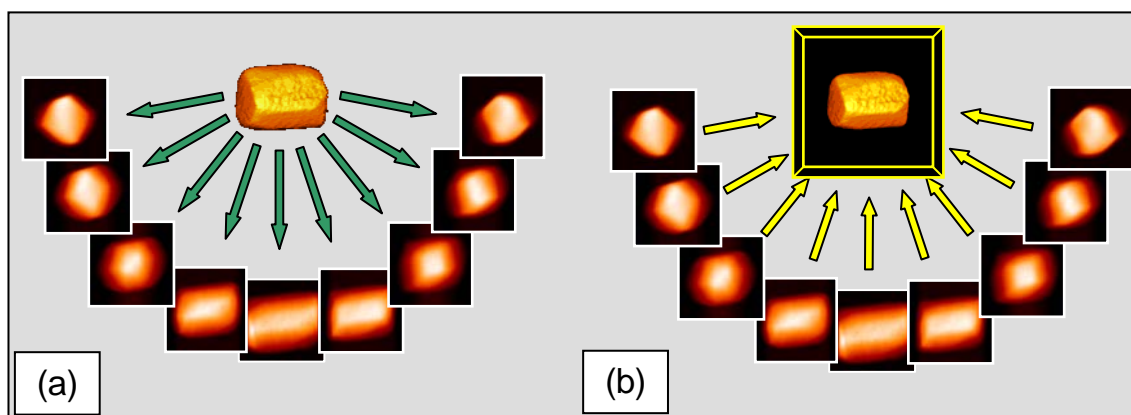


Figure 1. A schematic of reconstruction via backprojection. (a) An object is sampled by projection from a range of angles and then (b) reconstructed by summing these projections at the original sampling angles into the object space.

Reconstructions using this form of backprojection appear blurred, with low frequencies enhanced and fine spatial detail reconstructed poorly. This is an effect of the uneven sampling of spatial frequencies brought about by recording a tilt series – there will be a proportionately greater sampling of data near the centre of Fourier space. It is possible to partially rebalance the frequency distribution in Fourier space by using a weighting filter composed of a radially

linear function in Fourier space, zero at the centre and maximum at the edge. This improved reconstruction approach is known as weighted back-projection. [12].

The fidelity of a reconstruction can be improved further by noting that each recorded image is in essence a ‘perfect’ reference projection. If an (imperfect) reconstruction is re-projected back along the original projection direction then, in general, the re-projections will not be identical to the original images. The difference can in turn be back-projected generating a ‘difference’ reconstruction, which can be used to correct the original reconstruction, to constrain it to match the original set of images. The comparison operation must be repeated iteratively until a ‘best’ solution is reached [13, 14]. Comparisons of reconstructions using backprojection and iterative methods show that some iterative methods, especially simultaneous iterative reconstruction technique (SIRT) appear to be more robust to the presence of noise.

4. ELECTRON TOMOGRAPHY

In general if the back-projection method is to be used for reconstruction, the intensity of an image should be a monotonic function of some projected physical quantity [15] – the so-called ‘projection requirement’. In electron microscopy there is a number of competing contrast mechanisms some of which, to varying extent, obey the projection requirement. For amorphous materials, the contrast in a conventional bright-field (BF) TEM image arises primarily from changes in specimen density or thickness and is therefore suitable for tomography [16]. Using phase contrast images is also possible for weakly scattering specimens as has been demonstrated with great success with cryo-tomography in which frozen-hydrated specimens are examined in a more ‘natural state’. For many crystalline materials though, there is no simple relationship between the image intensity and the physical properties of the specimen because of the strong dynamical interactions between the electron beam and the crystal potential. In general, reconstructions, especially from BF images, can show artefacts and poor resolution of internal structure. To combat these problems, alternative imaging and contrast modes which satisfy the projection requirement have been developed.

It is evident that the reconstruction quality improves by including more images (projections) in the reconstruction. However, in practice, the number of images which can be acquired in the electron microscope is limited. The long exposure to the electron beam increases the likelihood of radiation damage. In addition, unlike many other tomography methods, electron tomography is undertaken in an instrument with a restricted working space and often it is impossible to tilt beyond a certain maximum angle, either because of the size of the pole-piece gap of the objective lens or because the specimen (if slab-like in morphology) becomes too thick. High specimen thicknesses will lead to a blurred image through chromatic aberration in TEM or beam broadening in STEM, and a degradation of contrast, brought about by increasing ‘absorption’. Thus in almost all electron tomography experiments there is a maximum tilt

angle beyond which there are no further projections and therefore there is a ‘missing wedge’ of information centred about the optic axis. One simple solution to overcome the restricted tilt range is to manufacture a fine ‘needle’ specimen, for example using a FIB workstation, to tilt the specimen about its own axis with an internal tilt mechanism [17], to allow complete 360° tilt of the specimen without shadowing and without an increase in projected thickness.

Although modern goniometers are very precise, it is inevitable that during acquisition of the tilt series the image will need to be re-positioned and re-focussed after each tilt. Automated acquisition schemes are now available for most electron microscopes, and focus can be corrected in TEM by measuring the image shift induced by a small beam tilt [18] and in STEM by maximising the image contrast [19]. Once the tilt series has been acquired, further alignment is needed to achieve high quality tomographic reconstructions. This is undertaken using fiducial markers or through cross-correlation techniques and tilt axis refinement [20, 21].

Assuming that the images recorded in the tilt series are spread evenly across 180°, the relationship between the number of projections, N , the diameter of the reconstruction volume, D and the overall resolution, d , has been estimated [22] as:

$$d = \frac{\pi D}{N} \quad (2)$$

There will be anisotropy in the spatial resolution brought about by the ‘wedge’ of missing information. The resolution is degraded most in the least-sampled direction and leads to an ‘elongation’ of the object in that direction (usually the optic axis), as illustrated in Fig. 2. An estimate of this elongation e , as a function of the maximum tilt angle α , [23] is:

$$e = \sqrt{\frac{\alpha + \sin \alpha \cos \alpha}{\alpha - \sin \alpha \cos \alpha}} \quad (3)$$

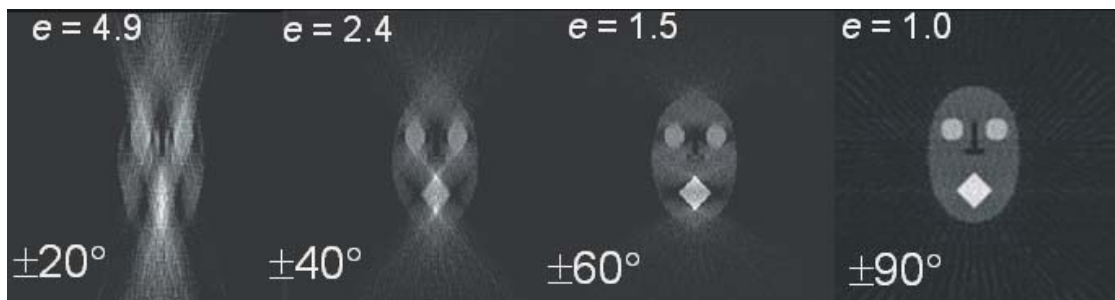


Figure 2. The elongation, e , of a reconstruction brought about by the maximum tilt angle (image courtesy of Dr. M. Weyland).

In the electron microscope, samples are often slab-like in morphology with far larger dimensions in-plane than in depth and D in eq. (2) should be modified to take this into account [24]:

$$D = t \cos \alpha \quad (4)$$

where t is the (un-tilted) thickness of the slab and α is the maximum tilt angle. As a consequence, fewer projections are required to attain the same overall resolution. Although these equations give an estimation of the expected tomographic resolution, in order to better quantify the resolution, the signal to noise ratio (SNR) of the images within the tilt series must be taken into account. One way is to use a Fourier shell correlation (FSC) method [25].

Further improvements to the reconstruction resolution can be made if the missing wedge of information is reduced to either a cone, through a conical tilting approach [26], or through a dual axis approach in which a second tilt series is recorded about a tilt axis perpendicular to the first. The latter has attracted more attention and novel reconstruction algorithms have been proposed which combine dual axis tomography with iterative reconstruction methods [27, 28]. Fig. 3 shows a graph indicating the fraction of information lost as a function of maximum tilt angle (a purely geometric calculation) for single and dual axis acquisition.

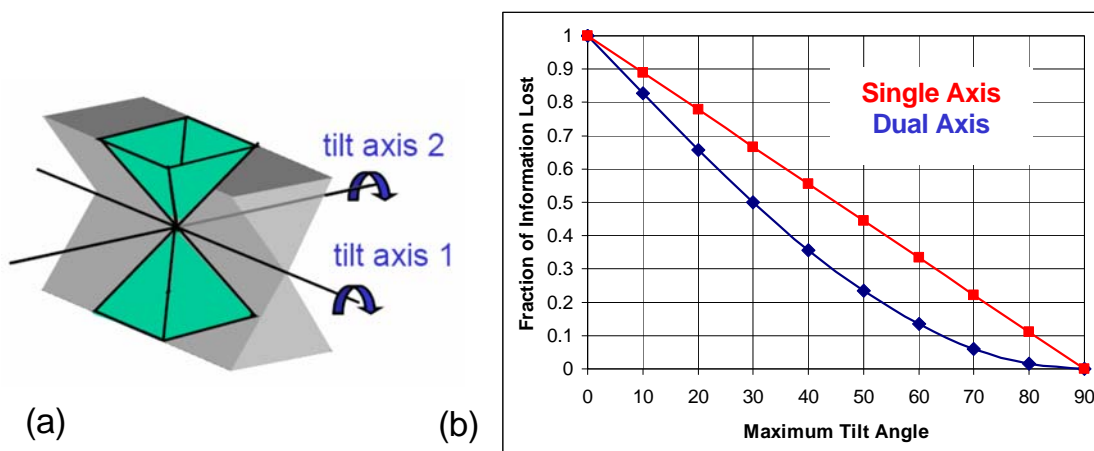


Figure 3. (a) A schematic illustration indicating the reduction of the missing wedge to a missing pyramid when a dual axis approach is taken to tomographic reconstruction. (b) A graph indicating the fraction of information lost for a single and dual axis acquisition for the same maximum tilt angle.

5. STEM HAADF TOMOGRAPHY

In the physical sciences there are a large number of imaging modes that can be used for tomographic reconstructions. Perhaps the most popular and useful is STEM HAADF imaging.

This type of imaging offers a number of advantages over conventional BF imaging for investigation of nanoscale objects and crystalline materials. The intensity of STEM images collected with a HAADF detector is a function of the projected thickness and the atomic number (Z) of the scattering object, approaching a Z^2 relationship for a detector annulus with a large inner radius. To a good approximation, such images represent a simple projection of the structure in terms of thickness and atomic number and therefore meet the projection requirement. Although STEM HAADF imaging is essentially incoherent in nature the image intensity can be modified by the orientation of a crystalline specimen: at a major zone axis, strong Bloch wave channelling tends to concentrate the beam intensity onto the atomic columns as it propagates through the crystal [29]. This increases the relative current density at atomic cores, increasing the high-angle scattering and consequently the intensity in the HAADF image [30].

However, it will be significant only at a relatively small number of orientations and thus the effect of channelling-enhanced contrast tends to have only a small effect on the overall tomographic reconstruction. Even for non-crystalline specimens with nanoscale features, the sensitivity of STEM HAADF imaging to atomic number is evident, as shown in Fig. 4 [31]. Here, a mesoporous silica catalyst is loaded with Ru-Pt nanoparticles about 1 - 2 nm in diameter; these are invisible in the conventional BF TEM image and are only seen when STEM HAADF imaging is used.

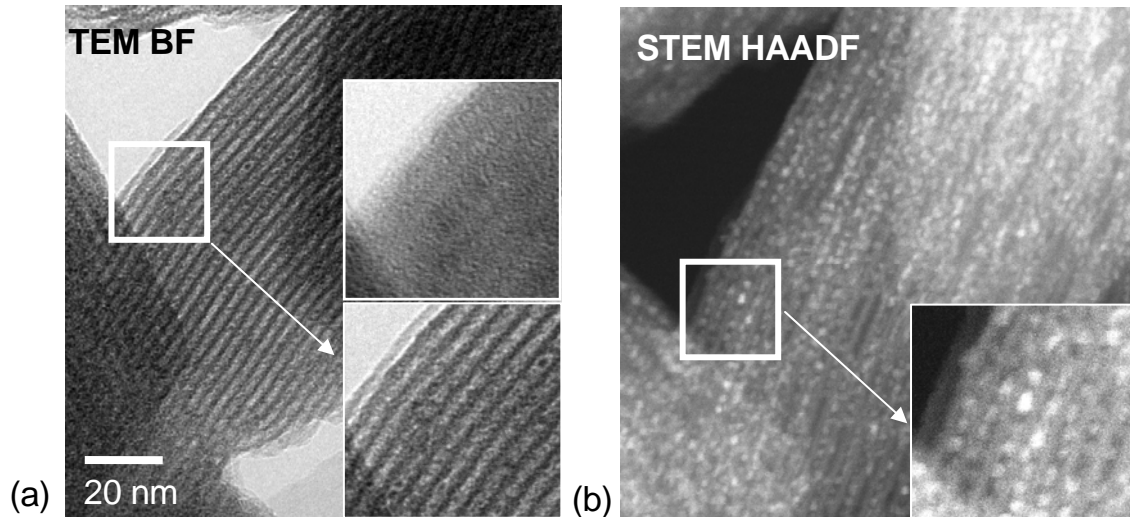


Figure 4. Images of mesoporous MCM41 silica. (a) An underfocus BF image showing ordered silica mesopores. The lower inset is a magnified part of the main image. The upper inset is the same magnified region but recorded in focus showing little amplitude contrast. (b) The same area of specimen as the image on the left but recorded as a STEM HAADF image; the pores can now be seen to be filled with Ru-Pt nanoparticles, invisible in the BF image.

For a standard specimen geometry (slab-like morphology), when tilted to high angles, only part of the specimen will be in focus. However, in STEM, a focal ramp can then be applied across the image to minimise problems associated with a limited depth of focus, a method known as ‘dynamic focusing’ used commonly in SEM. For very thick or specimens with high mass-density, with large average scattering angles, a significant proportion of scattering may fall outside the outer edge of the detector and lead to contrast reversals, and strong deviation from monotonic behaviour [32].

Fig. 5 is an example of STEM HAADF tomography applied to biogenic crystals. It shows a tomographic reconstruction of part of the ‘backbone’ of a magneto-tactic bacterium, strain MV-1 [33]. These bacteria have a chain of magnetite crystals which are aligned to allow the bacterium to sense the earth’s magnetic field. Electron tomography has enabled the crystal facets to be revealed with high fidelity and with high resolution [34].

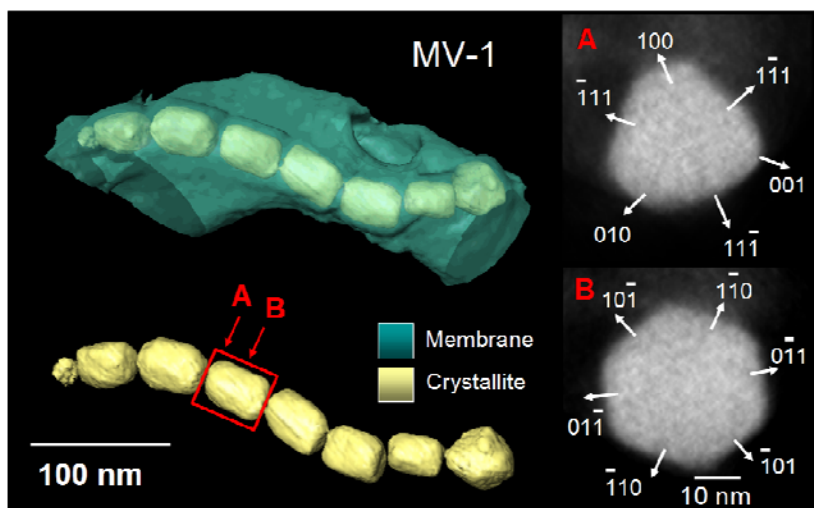


Figure 5. Left: A tomographic reconstruction of magneto-tactic bacteria strain MV-1. The chain of magnetite crystals is evident. Right: Slices taken through a single magnetite crystal in the chain reveal the perfect crystal faceting of the cubic crystals.

6. EFTEM TOMOGRAPHY

Energy-filtered transmission electron microscopy (EFTEM) is based on acquiring a series of energy-filtered images near an ionisation edge of interest, or sometimes at a plasmon feature. 2D compositional information from energy loss images may be isolated by generating either a background-subtracted elemental map or a jump-ratio map. Accounting for inelastic cross-sections, these maps can show intensity that is related to the concentration of an atomic species and, for relatively thin specimens, less than an inelastic mean free path thick, EFTEM maps

fulfil the projection requirement. One factor to bear in mind with EFTEM is the effect of prolonged electron exposure [35], but if the total dose is carefully controlled then EFTEM tomography can be applied even to highly beam sensitive biological specimens, to map for example phosphorous-containing ribosomes [36].

A simple but illustrative example of EFTEM tomography is shown in Fig. 6. Here an EFTEM tilt series has been acquired from a chain of nanospheres composed of an iron-nickel alloy which has oxidised [34]. The question was whether the spheres had sintered together and then the whole ensemble oxidised or whether the spheres had first oxidised and then agglomerated into the chain. From a single EFTEM map, colour coded in Fig. 6a it appears that the oxide shell is present between the spheres. However, after reconstruction of the oxygen tomogram, and taking a central slice through the sphere chain, it becomes evident that the metal spheres had sintered together first and then whole chain oxidised afterwards. Although a simple example, it highlights the potential of this form of 3D compositional tomography.

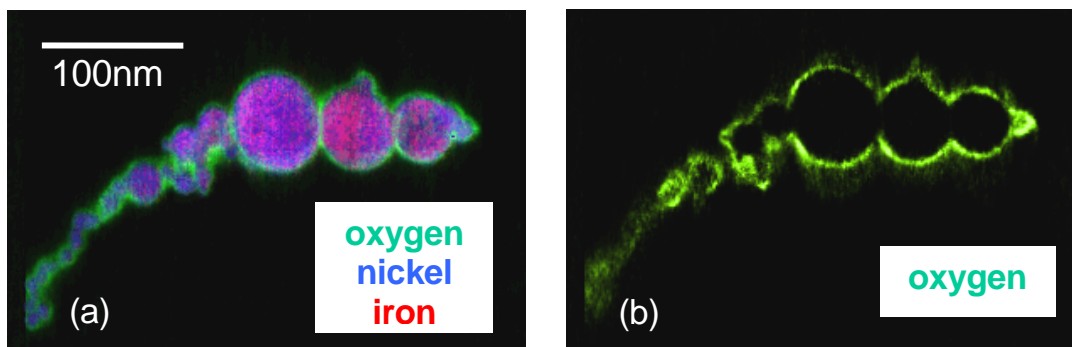


Figure 6. Left: RGB voxel projection of the combined reconstructions of a chain of FeNi nanoparticles. Right: A slice through the oxygen tomographic reconstruction showing how the oxide covers the ensemble of nanoparticles rather than individual nanoparticles.

If a series of energy loss images is acquired over an extended energy loss range, fully quantitative elemental maps can be generated [37]. By combining an energy loss series with a tomographic tilt series, a large four-dimensional dataset ($x, y, z, \Delta E$) is acquired. The 4D data set can be interrogated and spectroscopic data can be extracted from sub-volumes, a technique known as ‘4D volume-spectroscopy’ [38].

7. 3D DISLOCATION IMAGING BY ELECTRON TOMOGRAPHY

Weak-beam dark field (WBDF) imaging is used to reveal images of dislocations and can be combined with tomography [39] to reveal dislocation networks in 3D. In the example here, a

tilt series of WBDF images was acquired from an epitaxial thin film of GaN which had a network of threading and in-plane dislocations brought about by cracks in the film. Imaging (diffraction) conditions must remain approximately constant throughout the tilt series for the images to remain interpretable and useful for tomographic reconstructions. In practice, the dislocation image will wander slightly with respect to the dislocation core because of subtle changes in the imaging conditions and elastic anisotropy; this will translate into a blurring of the final reconstruction. Fig. 7 shows the result of a tomographic reconstruction of the GaN epilayer viewed from an oblique angle. It is evident that some threading dislocations, originating at the substrate-film interface, turn over part way through the film. ‘Rings’ of dislocations bound misorientation domains, often seen in GaN films.

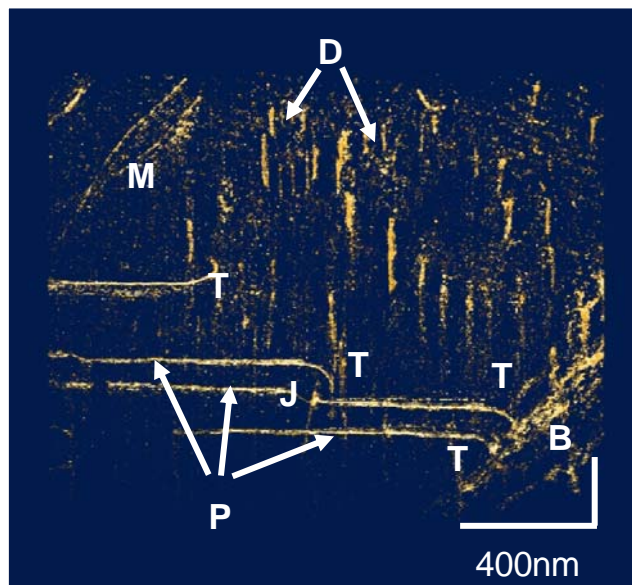


Figure 7. A WBDF tomographic reconstruction of a 3D dislocation network in a GaN epilayer film: P – in-plane dislocations; D – threading dislocations bounding domains; M – mixed dislocations; T – threading dislocations that have turned over to become in-plane dislocations; B – dislocation bundle; J – dislocation jog.

8. ELECTRON HOLOGRAPHIC TOMOGRAPHY

Electron holography can be combined with electron tomography to enable the 3D reconstruction of an electrostatic potential [40]. Fig. 8 shows a reconstruction of the 3D potential near a p-n junction in a specimen fabricated using a FIB workstation. The electronic properties of the doped crystalline silicon have been disrupted well below the surface. A tilt series of electron holograms were recorded and the unwrapped phase images reconstructed from the electron holograms were used for the reconstruction. Away from strong diffraction conditions, the reconstructed phase is directly proportional to the product of the potential and the projected thickness, and is thus suitable for reconstruction. The contrast across the

p-n junction arises because of the built-in potential. In this example the depletion region increases near the surfaces indicating a depletion of charge carriers which may arise by dopants pinned near the Fermi level by vacancies or interstitials created through knock-on damage initiated by the gallium beam.

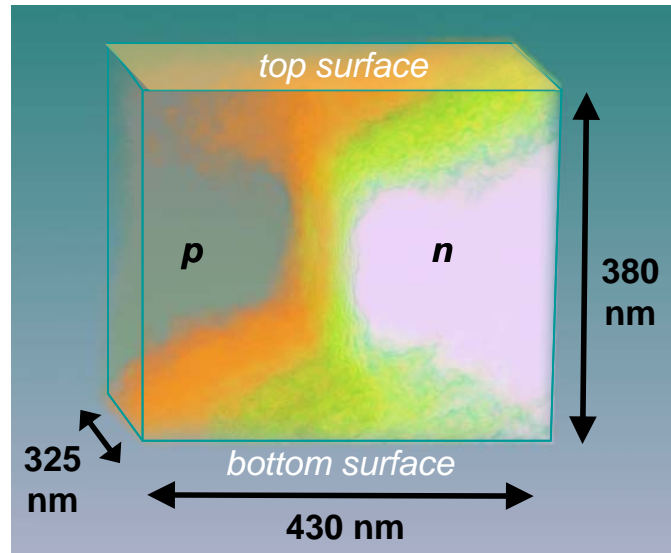


Figure 8. The 3D electrostatic potential, reconstructed from a series of holograms, shows an increasing depletion width near the surface of a p-n junction in a silicon device. The colour gradation represents changes to the electrostatic potential across the junction (image courtesy of Dr. A. Twitchett-Harrison).

9. CONCLUSIONS

Electron tomography is now a valuable tool to elucidate 3D structure, composition and physical properties over a wide range of materials and devices. The rise of nanotechnology brings with it the need to characterise nanoscale devices in three dimensions and in a quantitative manner. With improvements in imaging and algorithms, electron tomography is well placed to become an analytical tool for genuine 3D nano-metrology.

10. ACKNOWLEDGEMENTS

I am grateful to many colleagues for contributions to the work presented here, including M. Weyland, I. Arslan, T.J.V. Yates, J.S. Barnard, J. Sharp, J. M. Thomas and A.C. Twitchett-Harrison. Financial support from the EPSRC and EU FP 6 program 026019 ESTEEM is acknowledged.

11. REFERENCES

- [1] Radon J (1917) *Ber. Verh. K. Sachs. Ges. Wiss. Leipzig, Math.-Phys. Kl.* **69**: 262.
- [2] Bracewell R N (1956) *Aust. J. Phys.* **9**: 297.
- [3] Cormack A M (1963) *J. Appl. Phys.* **34**: 2722.
- [4] Hounsfield G N (1972) A method and apparatus for examination of a body by radiation such as X or gamma radiation. London, The Patent Office.
- [5] de Rosier D J and Klug A (1968) *Nature* **217**: 130.
- [6] Hoppe W, Langer R, Knesch G and Poppe C (1968) *Naturwissenschaften* **55**: 333.
- [7] Hart R G (1968) *Science* **159**: 1464.
- [8] Deans S R (1983) The Radon transform and some of its applications. New York/Chichester, J. Wiley and Sons.
- [9] Ramachandran G N and Lakshminarayanan A V (1971) *Proc. Nat. Acad. Sci.* **68**: 2236.
- [10] Radermacher M (1992) in: Electron tomography : three-dimensional imaging with the transmission electron microscope (Frank J, ed.). New York/London, Plenum Press, 91-116.
- [11] Herman G T (1980) Image reconstruction from projections, the fundamentals of computerised tomography. New York, Academic Press.
- [12] Gilbert P F C (1972) *Proc. R. Soc. Lond. B.* **182**: 89.
- [13] Crowther R A and Klug A (1971) *J. Theor. Biol.* **32**: 199.
- [14] Bellman S H, Bender R, Gordon R and Rowe J E (1971) *J. Theor. Biol.* **32**: 205.
- [15] Hawkes P W (1992) in: Electron tomography: three-dimensional imaging with the transmission electron microscope (Frank J, ed.). New York/London, Plenum Press, 17.
- [16] Spontak R J, Williams M C and Agard D A (1988) *Polymer* **29**: 387.
- [17] Koguchi M, Kakibayashi H, Tsuneta R, Yamaoka M, Niino T, Tanaka N, Kase K and Iwaki M (2001) *J. Electron Microscopy* **50**: 235.
- [18] Koster A J, Van Den Bos A and van der Mast K D (1987) *Ultramicroscopy* **21**: 209.
- [19] Kübel C, Voigt A, Schoenmakers R, Otten M, Su D, Lee T-C, Carlsson A and Bradley J (2005) *Microscopy and Microanalysis* **11**: 378.
- [20] Lawrence M C (1992) in: Electron tomography: three-dimensional imaging with the transmission electron microscope (Frank J, ed.). New York/London, Plenum Press, 197.
- [21] Midgley P A and Weyland M (2003) *Ultramicroscopy* **96**: 413.
- [22] Crowther R A, de Rosier D J and Klug A (1970) *Proc. Roy. Soc. Lond. A.* **317**: 319.
- [23] Radermacher M and Hoppe W (1980) Proceedings of the 7th European Congr. Electron Microscopy. Den Haag.
- [24] Radermacher M (1992) in: Electron tomography: three-dimensional imaging with the transmission electron microscope (Frank J, ed.). New York/London, Plenum Press, 91.
- [25] van Heel M and Harauz G (1986) *Optik* **73**: 119.
- [26] Mastrorarde D N (1997) *J. Struct. Biol.* **120**: 343.
- [27] Arslan I, Tong J R and Midgley P A (2006) *Ultramicroscopy* **106**: 994.

- [28] Tong J, Arslan I and Midgley P A (2006) *J. Struct. Biol.* **153**: 55.
- [29] Hirsch P B, Howie A, Nicholson R B, Pashley D W and Whelan M J (1977) *Electron microscopy of thin crystals*; 2nd ed. New York, Krieger.
- [30] Pennycook S J and Nellist P D (1999) in: *Impact of electron and scanning probe microscopy on materials research* (Rickerby D G, ed.). Kluwer, 161.
- [31] Thomas J M, Midgley P A, Yates T J V, Barnard J S, Raja R, Arslan I and Weyland M (2004) *Angew. Chem., Int. Ed.* **43**: 6745.
- [32] Dunin-Borkowski R E, Newcomb S B, Kasami T, McCartney M R, Weyland M and Midgley P A (2005) *Ultramicroscopy* **103**: 67.
- [33] Buseck P R, Dunin-Borkowski R E, Devouard B, Frankel R B, McCartney M R, Midgley P A, Posfai M and Weyland M (2001) *Proc. Nat. Acad. Sci.* **98**: 13490.
- [34] Weyland M, Yates T J V, Dunin-Borkowski R E, Laffont L and Midgley P A (2006) *Scripta Mat.* **55**: 29.
- [35] Egerton R F (1999) *J. Electron Microscopy* **48**: 711.
- [36] Leapman R D, Fiori C E, Gorlen K E, Gibson C C and Swyt C R (2004) *Ultramicroscopy* **100**: 115.
- [37] Thomas P J and Midgley P A (2001) *Ultramicroscopy* **88**: 179.
- [38] Gass M H, Koziol K, Windle A H and Midgley P A (2006) *Nano Letters* **6**: 376.
- [39] Barnard J S, Sharp J, Tong J R and Midgley P A (2006) *Science* **313**: 319.
- [40] Twitchett-Harrison A C, Yates T J V, Newcomb S B, Dunin-Borkowski R E and Midgley P A (2007) *Nano Letters* **7**: 2020.

